

Ionization, dust, and Mg II emission: understanding the spatial variation of photon escape in a local LyC leaker

Thomas Seive,¹★ John Chisholm,¹ Floriane Leclercq,¹ Gregory Zeimann,¹

¹*Department of Astronomy, University of Texas, Austin, TX 78712, USA*

Accepted XXX. Received YYY; in original form ZZZ

ABSTRACT

Ionizing photons must have escaped from high-redshift galaxies, but the neutral high-redshift intergalactic medium makes it unlikely to directly detect the escape of ionizing photons during the epoch of reionization. Indirect methods of studying ionizing photon escape fractions present a way to infer escape fractions and understand how ionizing photons escape from the first galaxies. Here, we use HET/LRS2 observations of J0919+4906, a confirmed low-redshift emitter of ionizing photons, to achieve spatially resolved spectroscopy of Mg II λ 2796, Mg II λ 2803, [O II] λ 3728, [Ne III] λ 3869, H γ , [O III] λ 4363, H β , [O III] λ 4959, [O III] λ 5007, and H α . From these data we measure Mg II emission, which is suspected to be an indirect tracer of ionizing photons, along with nebular ionization and dust attenuation in multiple spatially-resolved apertures. J0919+4906 has significant spatial variation in its Mg II escape and thus ionizing photon escape fraction. Combining our observations with photoionization models, the regions with the largest relative Mg II emission and Mg II escape fractions have the highest ionization and lowest dust attenuation. Some regions have nearly unity escape fraction, while other regions transmit very little ($\sim 10\%$) of their intrinsic Mg II emission. Dust absorbs more Lyman Continuum photons than Mg II photons such that regions with high attenuation and low Mg II escape have even smaller Lyman Continuum escape fractions. We compare the spatially-integrated Mg II and ionizing photon escape fractions to individual sight lines and find that the integrated escape is similar to the average of all of the individual regions, but there exists substantial scatter. For example, the integrated aperture has an order of magnitude fewer ionizing photons than the central aperture. This makes the integrated escape fraction lower than the value typically quoted as being sufficient to reionize the universe, even though the central value is higher. Single sight-line observations may not trace the volume-averaged escape fraction of ionizing photons which may introduce significant scatter into the indirect tracers of ionizing photon escape.

Key words: keyword1 – keyword2 – keyword3

1 INTRODUCTION

Between redshifts of 5–10, the intergalactic medium in the early universe rapidly went through a phase transition from neutral to ionized (Becker et al. 2001; Fan et al. 2006; Bañados et al. 2017). This ionization was brought about by Lyman Continuum (LyC) photons which have $\lambda < 912 \text{ \AA}$. Understanding the source of these photons means understanding the timing, duration, and overall evolution of large scale structure in the universe (Robertson et al. 2013; Madau & Dickinson 2014; Robertson et al. 2015). Furthermore, the process of understanding the sources of ionizing photons has many profound questions that have far reaching consequences beyond the reionization of the universe.

Initially, the debate around the sources of reionization centered around whether active galactic nuclei (AGN) or massive stars were most responsible for providing ionizing photons (Oesch et al. 2009; Faucher-Giguère et al. 2009; Robertson et al. 2013; Madau & Haardt 2015). AGN generate many ionizing photons and are concentrated in the depths of gravitational potentials. However, observations find that there are too few AGNs to reionize the universe (Hopkins et al. 2008;

Onoue et al. 2017; Ricci et al. 2016; Matsuoka et al. 2018; Shen et al. 2020). On the other hand, star forming galaxies are readily observed at the required redshifts and are broadly distributed spatially. In order to be star forming, they must have large amounts of cold gas. This cold, neutral gas will efficiently absorb ionizing photons, thereby reducing the amount of photons that escape a typical star-forming galaxy. This property of star forming galaxies has shifted the current debate to whether widely distributed low-mass galaxies or heavily clustered bright massive galaxies were the sources of ionizing photons (Finkelstein et al. 2019; Naidu et al. 2020; Matthee et al. 2021). (Might be worth adding in a sentence on the escape fractions needed to reionize the universe)

The amount of ionizing photons that escape a source, known as the emissivity (J_{ion} [photon $\text{s}^{-1} \text{ Mpc}^{-3}$]), requires measurements of the density of sources and the production of ionizing photons of each source. J_{ion} can be numerically represented as

$$J_{\text{ion}} = f_{\text{esc}}(\text{LyC}) \xi_{\text{ion}} \rho_{\text{UV}} \quad (1)$$

where $f_{\text{esc}}(\text{LyC})$ is the fraction of ionizing photons that escape a galaxy, ξ_{ion} is the intrinsic production of ionizing photons per FUV luminosity for each source, and ρ_{UV} is the FUV luminosity function. Observing all of these parameters for star forming galaxies in the

★ E-mail: thomasseive@utexas.edu

Epoch of Reionization (EOR) would answer how the Universe evolved. Unfortunately, all of these parameters have their own challenges associated with measuring them, with escape fractions being the most uncertain of them.

Observations have found that $f_{\text{esc}}(\text{LyC})$ must be $> 5\text{--}20\%$ in order for star forming galaxies to reionize the universe (Ouchi et al. 2009; Robertson et al. 2013, 2015; Finkelstein et al. 2019; Naidu et al. 2020). Locally, where the IGM is fully ionized and the escape fraction can be measured directly, $f_{\text{esc}}(\text{LyC})$ is often found to be less than 5% (Grimes et al. 2009; Vanzella et al. 2010; Leitherer et al. 2016; Naidu et al. 2018). However, doing similar observations of escape fractions at redshifts between now and the EoR would be difficult because of intervening neutral gas. This obstruction calls for indirect observables of $f_{\text{esc}}(\text{LyC})$.

We can calibrate and determine methods of LyC escape in an empirical manner. Thus far, these methods have included Ly α emission properties (Verhamme et al. 2015; Rivera-Thorsen et al. 2017; Izotov et al. 2018; Gazagnes et al. 2021; Izotov et al. 2021), ISM absorption properties (Reddy et al. 2016; Gazagnes et al. 2018; Chisholm et al. 2018; Steidel et al. 2018), resonant emission lines (Henry et al. 2018; Chisholm et al. 2020; Witstok et al. 2021), and optical emission line ratios (Nakajima & Ouchi 2014; Oey et al. 2014; Wang et al. 2019), all with appreciable scatter and their own drawbacks. For example, metal absorption lines require deep observations to detect the stellar continuum (Chisholm et al. 2018; Steidel et al. 2018; Jaskot et al. 2019). One possible solution is that there is substantial variation in the escape fraction from sight line to sight line such that optically thin and optically thick tracers are encountering very different LyC escape fractions.

Here we aim to test the spatial variation of the neutral gas opacity in a previously confirmed LyC emitting galaxy. We use spatially resolved IFU observations to determine Mg II and other emission lines to test if spatial variation in a target can lead to substantial variation in sight line to sightline escape fractions. In section 2 we describe the LRS2 observations and data reduction. section 3 describes our process for extracting emission line parameters and draws similarities and differences to other observations in the literature. Our observations of the dust, ionization, and Mg II emission are described in section 4. We conclude in section 5 by exploring the implications of our measurements on single sight-line observations.

2 OBSERVATIONS AND REDUCTIONS

2.1 Observations

We observed J0919+4906 (RA: 09:19:55.78, Dec: +49:06:08.75) over 3 nights (January 8th 2021, January 9th 2021, and March 3rd 2021) with four total exposures using the LRS2 spectrograph (Chonis et al. 2014) on the Hobby-Eberly Telescope. Three of the exposures had an exposure time of 1800 seconds using the LRS2-B configuration. The fourth exposure had an exposure time of 500 seconds with the LRS2-R configuration. This object is of interest because it was one of the recently discovered Lyman Continuum (LyC) emitters from Izotov et al. 2021. The maximum seeing was $\approx 2.6''$ and the spatial scale of the observations was $0.25''$ by $0.25''$ per spaxel. The spectral resolution of the observation depends on the LRS2 spectrograph arm (UV: 1.63\AA , Orange: 4.44\AA , Red: 3.03\AA , Farred: 3.78\AA).

This object has been observed with the SDSS in the optical (Aguado et al. 2019) and HST/COS in the FUV (Izotov et al. 2021). These observations supplement our work. The SDSS observation

provides values to compare against the LRS2 observations (subsection 3.6). From our central aperture (Figure 1), we measure a Signal to Noise Ratio (SNR) of 70 in [O II] $\lambda 3728$, which is one of our weakest emission lines. This SNR is ~ 2 times higher than the SNR of 38 from the SDSS for the same line. The HST/COS observations provide a direct measurement of the LyC escape fraction. The LyC escape fraction is a value we attempt to indirectly measure in this work.

2.2 Data reduction

The HET observations reported here were obtained with the LRS2 spectrograph. LRS2 comprises two spectrographs separated by 100 arcseconds on sky: LRS2-B (with wavelength coverage of $3650\text{\AA} - 6950\text{\AA}$) and LRS2-R (with wavelength coverage of $6450\text{\AA} - 10500\text{\AA}$). Each spectrograph has 280 fibers covering $6'' \times 12''$ with nearly unity fill factor (Chonis et al. 2014). We used the HET LRS2 pipeline, Panacea¹, to perform the initial reductions including :fiber extraction, wavelength calibration, astrometry, and flux calibration. There are two channels for each spectrograph: UV and Orange for LRS2-B and Red and Farred for LRS2-R. On each exposure, we combined fiber spectra from the two channels into a single data cube accounting for differential atmospheric refraction. We then identified the target galaxy in each observation and rectified the data cubes to a common sky coordinate grid with target at the center.

We first smoothed each cube to the worst seeing conditions of the four observations. To normalize each cube, we measured H β in both LRS2-B and LRS2-R at the observed wavelength of $\approx 6831\text{\AA}$. After normalization we stacked the individual cubes together using a variance weighted mean. In subsection 3.6, we check the flux calibration by comparing the line ratios of the SDSS and LRS2 spectra and find offsets ranging from 0σ to 3σ between the two observations.

3 EMISSION LINE PARAMETER ESTIMATION

Here we describe the techniques used to derive emission line properties from the observations described in subsection 2.1. We first defined apertures for the spectral extraction (subsection 3.1), removed the continuum from the spectra (subsection 3.2), fit the emission lines (subsection 3.3), and corrected for dust attenuation (subsection 3.4). Our analysis was primarily done using the SPECUTILS, SPECTRALCUBE (Astropy Collaboration et al. 2018), and LMFIT (Newville et al. 2014) python packages.

3.1 Apertures

A primary goal of this work is to test the impact of geometry and spatial distribution on the resonant Mg II emission. To do this, we extract the spectral information from spatially distinct apertures within the LRS2 data cube that are separated by more than the convolved seeing of the observations. Doing this leaves us with 5 spaxel radius (1.25 arcsec) apertures, as dictated by the seeing of the observations in subsection 2.1. Given this aperture size, we optimized the number of apertures while maximizing the delivered signal-to-noise by extracting our signal from four spatially distinct regions. These regions covered the extent of J0919 without sampling the center multiple times, as seen in Figure 1.

While the center-most aperture (radius of 1 arcsec) does overlap

¹ <https://github.com/grzeimann/Panacea>

with the other apertures, it allows for the LRS2 data to be compared to other data sets in the literature. The large aperture, referred to as the "Integrated aperture", maximizes the SNR of our observations. We extracted the spectra by summing the flux in each aperture. Figure 2 shows the lines we extracted from our spatially distinct apertures.

3.2 Continuum fit

To ensure the measured emission line properties did not contain contributions from the stellar and nebular continua, we first had to remove the continuum. For our continuum fitting procedure, we used the `FIT_CONTINUUM` function from the `SPECUTILS` package. We modified the default Chebyshev model to be 1st order instead of 3rd order to better match the observed continuum shape. In order to fit the continuum, we visually picked a region on either side of the emission line that was in close proximity to the line but did not contain any absorption/emission features. This procedure was applied to the spectra extracted in the different apertures. The residual emission flux was then obtained by subtracting the resulting continuum models.

Stellar population models suggest that young stellar populations have a $\sim 2 \text{ \AA}$ $H\beta$ equivalent width (González Delgado et al. 1999). J0919 has a measured $H\beta$ equivalent width of 435 \AA (Izotov et al. 2021). This extreme value indicates that the stellar population is very young. The change in $H\beta$ equivalent width caused by stellar population models would be of less than 0.5% for J0919. Further, with the continuum not being significantly detected underneath the Balmer lines (see Figure 3 bottom row, third panel), we conclude that there is little contribution from stellar absorption.

3.3 Emission line fit

Our method to measure the emission line parameters consisted of using `LMFIT` and a bootstrap Monte Carlo method. More precisely, we use the `MINIMIZE()` function and a Gaussian model with parameters of line center, line width, and amplitude to achieve all of our fits. The lower limit for the line width of our fits was based on the spectral resolution of each LRS2 arm (see subsection 2.1 for the limits). This work focuses on the integrated fluxes. Subsequent work will study the kinematic information of the emission lines.

For our bootstrap Monte Carlo method, we first calculated the standard deviation by using the continuum-subtracted flux and 80-100 pixel-wide windows directly adjacent to each individual emission line. With the `NUMPY.RANDOM.NORMAL()` function (Harris et al. 2020), we generated 1000 realizations of the extracted spectrum where each flux density is randomly drawn from a normal distribution centered on the original flux density value with a standard deviation given by the estimated noise value calculated above (a bootstrap Monte Carlo method). We then fit a Gaussian to each of the 1000 modified spectra (see subsection 3.2). Our initial values came from the `SPECUTILS.FIND_LINES.THRESHOLD` function.

We tabulated the results and took the mean and standard deviation of the distribution. The results of these calculation are reported in Table 1. These techniques allowed us to measure the properties and errors of the emission lines of interest in a consistent way. Examples of our fits can be found in Figure 3. Table 1 gives the observed and extinction corrected fluxes (subsection 3.4), respectively, for 9 different measured emission lines in our 6 different apertures.

All conversions from wavelengths to velocities were done using the restframe wavelengths from the NIST Atomic Spectra Database Lines Form (Kramida et al. 2021). The lines measured in this work were Mg II , $[\text{O II}]\lambda 3728$, $[\text{Ne III}]\lambda 3869$, $\text{H}\gamma$, $[\text{O III}]\lambda 4363$, $H\beta$, $[\text{O III}]\lambda 4959$, $[\text{O III}]\lambda 5007$, and $H\alpha$.

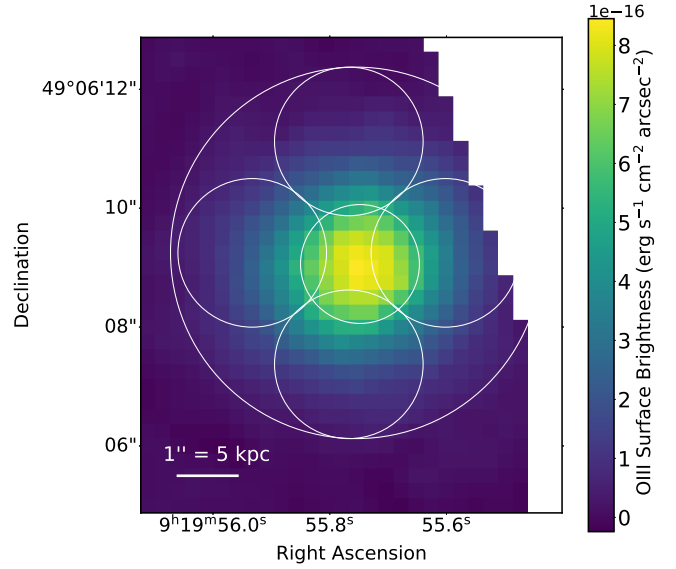


Figure 1. The continuum subtracted surface brightness spatial map for $[\text{O III}]\lambda 5007$. The largest aperture is referred to as the Integrated aperture and the others are named after their position relative to the galaxy center (e.g. the aperture at the top of the image is the Top aperture). We include a 1" scale bar, where 1" corresponds to approximately 5 kpc in the frame of the galaxy.

3.4 Dust extinction correction

We corrected the continuum subtracted emission-line flux values to account for the impact of dust present in the Milky Way (MW) and J0919. Dust extinction reduces the amount of flux that reaches our telescope by absorbing and/or scattering the photons of interest. It is also wavelength dependent meaning very blue lines, like Mg II , are more reduced than redder lines like $H\beta$. Correcting for dust extinction and comparing to uncorrected values constrains the spatial distribution of dust and reveals the intrinsic nebular conditions (e.g. metallicity, ionization structure, etc.). The correction was done using the following steps:

(i) Corrected the flux based on J0919's position in the Milky Way (MW) by multiplying the flux by:

$$10^{0.4 \times E(B-V)_{\text{MW}} \times k(\lambda_{\text{obs}})}, \quad (2)$$

where $E(B-V)_{\text{MW}}$ is the MW color excess, which has a value of 0.029 (Green et al. 2019), and $k(\lambda_{\text{obs}})$ is the value of the CCM89 extinction law at the observed wavelength of each individual emission line (Cardelli et al. 1989).

(ii) Calculated the color excess from J0919 using equation A8 from (Rosa-González et al. 2002)

$$E(B-V) = \frac{\log 0.47 - \log \frac{F(\text{H}\gamma)}{F(\text{H}\beta)}}{0.4[k(F(\text{H}\gamma)) - k(F(\text{H}\beta))]} \quad (3)$$

We determine $E(B-V)$ using $F(\text{H}\gamma)$ and $F(\text{H}\beta)$, which are the continuum subtracted and MW dust attenuation corrected $\text{H}\gamma$ and $\text{H}\beta$ fluxes from each aperture. The value of 0.47 is the intrinsic $\frac{\text{H}\gamma}{\text{H}\beta}$ ratio with no dust attenuation (Osterbrock 1989). This value assumes a temperature of 10^4 K and a density of 100 cm^{-3} . The values of $k(\text{H}\gamma)$ and $k(\text{H}\beta)$ are the values of the CCM89 extinction law at the rest wavelength values of $\text{H}\gamma$ and $\text{H}\beta$ (4340 \AA and 4861 \AA respectively). See Table 1 for the $E(B-V)$ values for each aperture. To avoid non-physical values, we capped the values of $E(B-V)$ to 0. This cap only affected the top aperture.

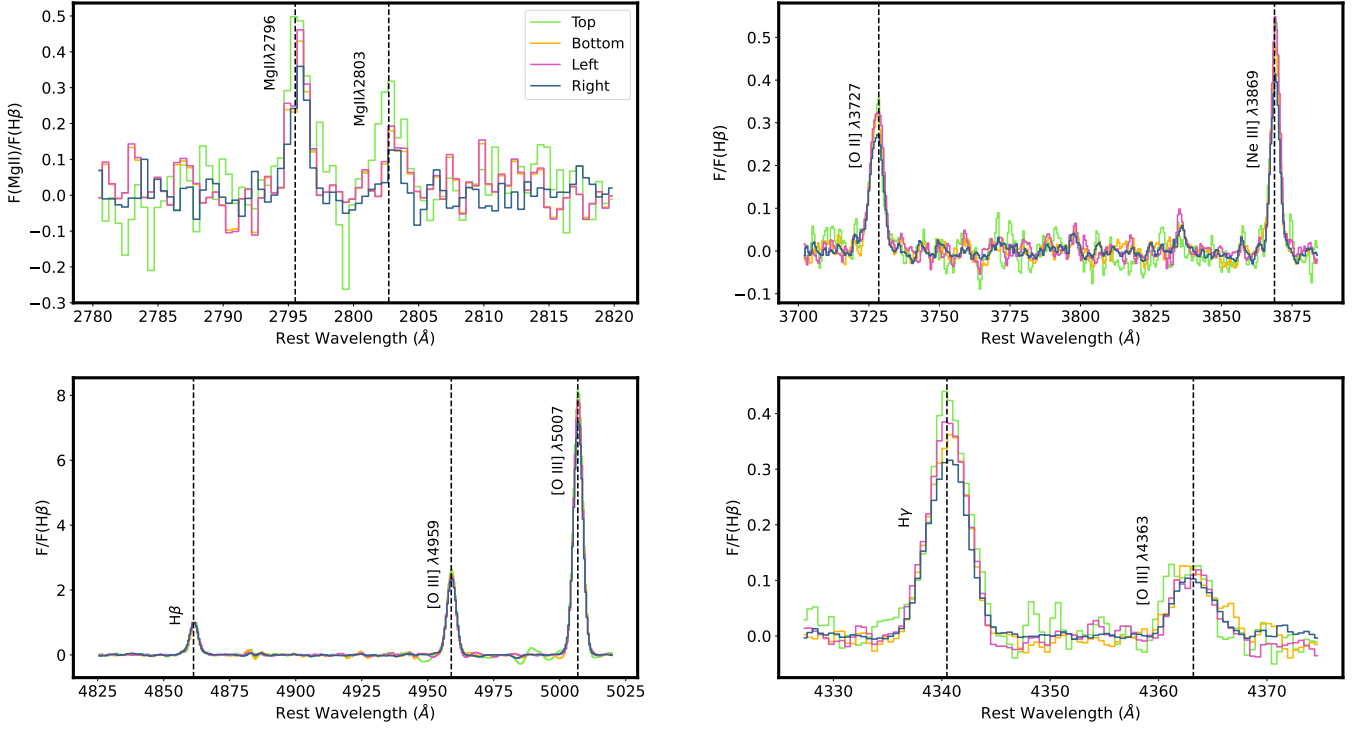


Figure 2. The restframe spectra of Mg II, [O II] $\lambda 3728$, [Ne III] $\lambda 3869$, H γ , [O III] $\lambda 4363$, H β , [O III] $\lambda 4959$, and [O III] $\lambda 5007$ from each aperture, overlaid on one another. The flux densities were continuum subtracted but not dust extinction corrected. The flux densities were normalized by the maximum H β flux density in their respective aperture such that all flux densities are relative to H β . The vertical dashed lines represent the rest wavelength line center.

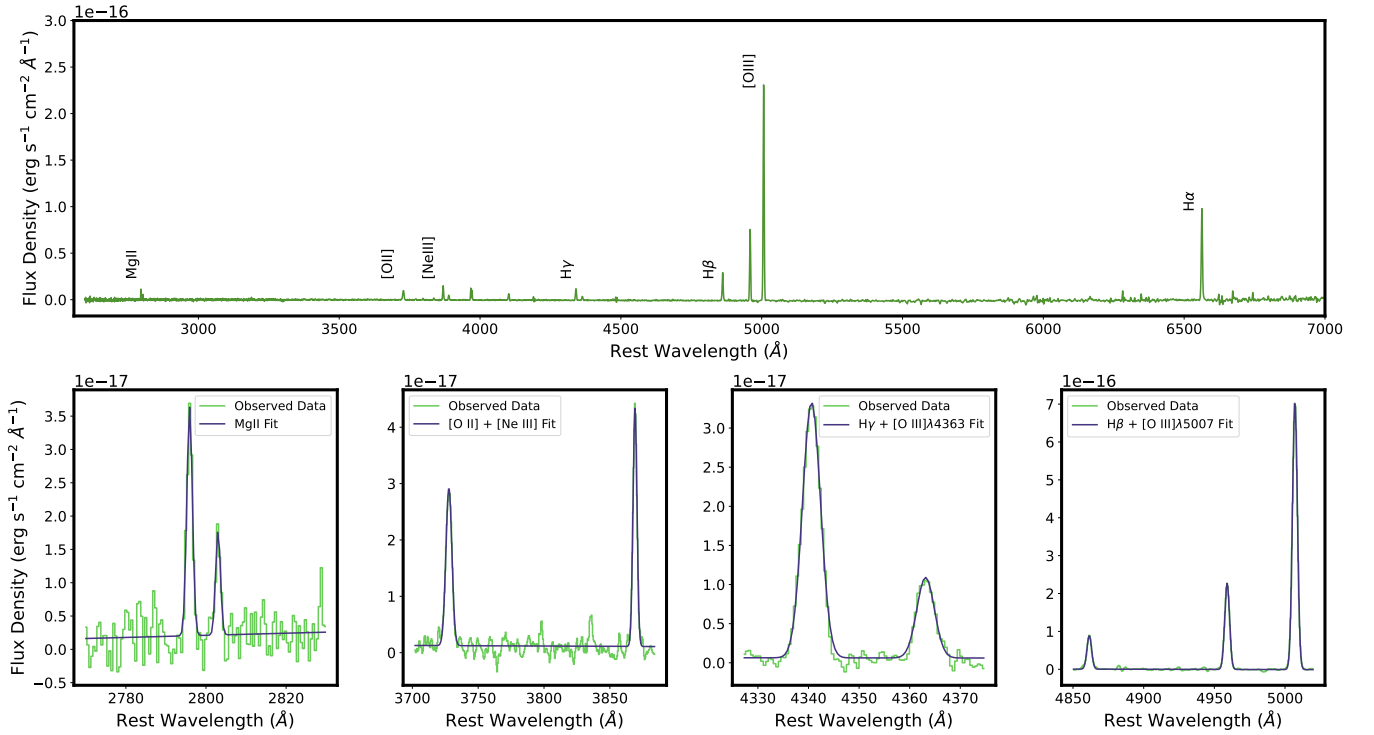


Figure 3. *Top:* the complete observed spectra from the Integrated aperture with a few lines of interest labelled. *Bottom:* A zoom in on some emission line fits with the observed spectra in green and the fit in purple. The lines that we fit are: Mg II, [O II] $\lambda 3728$, [Ne III] $\lambda 3869$, H γ , [O III] $\lambda 4363$, H β , [O III] $\lambda 4959$, [O III] $\lambda 5007$, and H α .

(iii) To correct for dust in J0919 we multiplied the MW corrected fluxes by:

$$10^{0.4 \times E(B-V) \times k(\lambda_{rest})} \quad (4)$$

We did not correct the values in the [O III] λ 5007 spatial map (see Figure 1) in order to retain the observed spatial extent of J0919. However, we did apply these corrections to all the rows marked with "Cor" in Table 1. This was done to highlight spatial differences between the apertures.

3.5 Determining metallicities

For each aperture we used PYNEB (Luridiana et al. 2014) and the extinction-corrected [O III] λ 5007, [O III] λ 4363, [O II] λ 3727 fluxes, all normalized by the H β flux, to calculate the Oxygen abundances using the direct- T_e method (Garnett 1992, Berg 2013). To determine the electron temperature, we used the temperature sensitive ratio of [O III] λ 5007 to the auroral [O III] λ 4363 line. Our calculated electron temperatures range from 14000-15804 K. We then used the [O II] λ 3727 and [O III] λ 5007 fluxes, relative to H β , to determine the oxygen abundances in the intermediate (for [O II] λ 3727) and high-ionization (for [O III] λ 5007) zone by assuming a single temperature across the H II region. By considering the total oxygen abundance as the sum of the intermediate and high ionization zones, we calculated the total oxygen abundance. This is a good approximation for galaxies that are as highly ionized as our target.

We detect the [O III] λ 4363 line at $> 4\sigma$ significance in all of our apertures and list the inferred metallicity in each aperture in the last column of Table 2 as $12 + \log(\text{O}/\text{H})$. Izotov et al. 2021 calculated an electron temperature of 16660 ± 1440 and a metallicity of 7.77 ± 0.01 . These values are 3σ from our measurements in the central aperture (Table 2).

3.6 Comparison to previous work

To compare the LRS2 observations presented here to other literature measurements, we extracted the LRS2 flux from a $2''$ aperture, centered on the peak emission within J0919 (called the central aperture; the center most aperture in Figure 1). This aperture matches the $2''$ diameter of the BOSS fibers (Smee et al. 2013). We then downloaded the calibrated spectra from the Sloan Digital Sky Survey DR15 (Aguado et al. 2019) and measured the emission line properties in the same way as was done in Sections 3.2-3.4 with the LRS2 data. Our values from the SDSS spectra match literature values for integrated flux, equivalent width, and $E(B-V)$ within 1.5σ for all emission lines (Flurry et al. submitted, Izotov et al. 2021).

Table 3 compares the emission line ratios measured from the LRS2 (top row) and SDSS (bottom row) spectra. Most of the values measured from LRS2 match what we measured from the SDSS. There are two exceptions. We measured a value of 3.95 for $\frac{H\alpha}{H\beta}$ from the LRS2 data. This is inconsistent with the value we measured from the SDSS data of 2.97. Our value for the [O III] λ 5007/[O II] λ 3728 ratio is also inconsistent with the SDSS measurement. Both the H α and [O III] λ 5007 lines are observed in the Red arm, while the other lines discussed here are on the Blue arm of LRS2. This suggests a slight flux calibration offset between the Blue and Red arms of LRS2. There may be a slight absolute flux calibration between the Red and the Blue arms making lines in the red arm appear brighter than the blue arm, however, the relative flux calibration appears to be robust and consistent across the apertures. This means that the offset in the flux ratios will be similarly offset within the LRS2 observations, but

may not be directly comparable to emission line measurements from other instruments.

To estimate the dust attenuation, it is crucial to have flux estimates on consistent flux scales. The H β and H γ lines are both observed in LRS2-Blue and the measured values for both the SDSS and LRS2 observations were found to be 0.44. This consistency indicates that the H γ and H β ratio can be used to infer the dust attenuation. This is why we used the $\frac{H\gamma}{H\beta}$ ratio instead of $\frac{H\alpha}{H\beta}$ to determine the dust attenuation. We used a redshift value of 0.40512 from SDSS in our calculations but most of the LRS2 emission lines are slightly offset from this systemic value (by $\sim 10 \text{ km s}^{-1}$). With our measurements matching other independent measurements, we can move forward assuming accurate results from our analysis.

4 RESULTS

In this section we use the continuum-subtracted Mg II λ 2796, H γ , and H β fluxes along with the continuum-subtracted, attenuation-corrected flux [O III] λ 5007 and [O II] λ 3728 to measure dust extinction, ionization, and Mg II λ 2796 flux. In the following subsections we compare ionization ([O III] λ 5007/[O II] λ 3728) to dust (H γ /H β), dust to Mg II λ 2796/[O III], and ionization to Mg II λ 2796/[O III] λ 5007. While our 6 apertures represent too small of a sample to be statistical, this analysis aims to quantify the spatial variation of Mg II within a single LyC emitting galaxy to assess the spatial variation of the LyC escape.

4.1 Ionization v. dust

Within the frame of understanding local LyC escape, we explored the relationship between ionization and dust in each aperture. Ionization is important for LyC escape because galaxies that are more ionized have less relative neutral hydrogen. We use the [O III] λ 5007/[O II] λ 3728 ratio because this ratio directly traces the fraction of highly ionized to moderately ionized gas. As such it is a diagnostic of the ionization state of the gas, with higher [O III] λ 5007/[O II] λ 3728 values corresponding to more highly ionized nebulae. Dust preferentially absorbs and scatters bluer wavelengths, meaning that it strongly absorbs ionizing photons. This relationship is shown in Figure 4. Our dust ratios consist of the observed H γ and H β fluxes, where a ratio of 0.47 represents a dust free nebulae (Osterbrock 1989). These uncorrected fluxes give us a direct measurement of the impact of dust. The [O III] λ 5007 and [O II] λ 3728 fluxes were corrected for dust attenuation because we were interested in the intrinsic ionization of the aperture. We measure different ionization and dust attenuation values for each aperture and find a negative trend between ionization and dust (note that dust content increases towards lower $\frac{H\gamma}{H\beta}$ values while ionization decreases towards lower values). This trend indicates that regions within J0919 with less dust are more highly ionized. We discuss the implications for this trend in subsection 5.1.

4.2 Dust v. Mg II λ 2796 flux

There are two sinks for ionizing photons: dust and gas. One of our goals is to explore the relative impact of both dust and neutral gas on a spatial basis within J0919. We can explore neutral gas using the Mg II doublet ratio or photoionization models (Henry et al. 2018, Chisholm et al. 2020). The two Mg II transitions (Mg II λ 2796 and Mg II λ 2803) have different oscillator strengths. This means that their observed

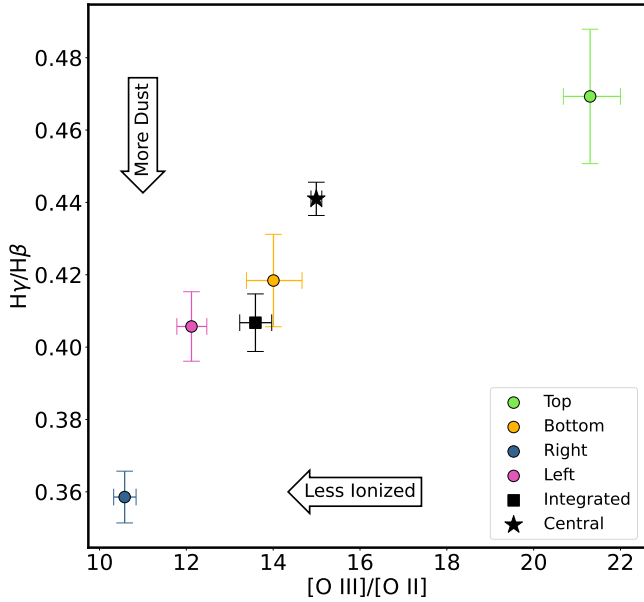


Figure 4. The $H\gamma/H\beta$ ratio of the individual apertures versus the $[O\text{ III}]\lambda 5007/[O\text{ II}]\lambda 3728$ ratio. The $H\gamma/H\beta$ ratio traces dust attenuation and the $[O\text{ III}]\lambda 5007/[O\text{ II}]\lambda 3728$ ratio traces ionization. Dust content increases with deviations from 0.47 (see arrows). The value of 0.47 corresponds to a dust free region. The legend caption refers to the aperture location.

relative flux ratios are sensitive to the Mg II column density. However, the SNR of Mg II λ 2803 is too low to allow for an analysis using the doublet ratio technique on a spatially resolved basis (see Table 1). Instead, we take the observed Mg II λ 2796 values and normalize them by the dust attenuation corrected $[O\text{ III}]\lambda 5007$ values. The fraction of Mg II λ 2796 emission we observe relative to the $[O\text{ III}]$ emission is related to the neutral gas column density. This enables us to study the relationship between neutral gas column density and the dust attenuation.

We measure different dust attenuation and Mg II λ 2796 flux values for each aperture. The Mg II λ 2796 line, normalized by the $[O\text{ III}]\lambda 5007$ line, is positively correlated with the $H\gamma/H\beta$ ratio (Figure 5). More Mg II λ 2796 relative to $[O\text{ III}]$ emission escapes the galaxy in less dusty regions of J0919. In Section 5.1 we use photoionization models to explore how this observation relates to the escape of ionizing photons.

4.3 Ionization v. Mg II λ 2796 flux

The ionization state of the gas traces the amount of low ionization relative to high ionization gas. In regions with high ionization there is less neutral gas that can absorb LyC photons and the Mg II λ 2796/ $[O\text{ III}]\lambda 5007$ ratio allows for a comparison between the observed Mg II values and the predicted values from the photoionization models of Henry et al. (2018) (see subsection 4.3).

In each of our apertures, we measure different ionization and Mg II λ 2796 flux values. Figure 6 shows a positive trend between ionization, measured with the dust attenuation corrected $[O\text{ III}]\lambda 5007/[O\text{ II}]\lambda 3728$ ratio, and the observed Mg II λ 2796 flux, which was normalized by the dust attenuation corrected $[O\text{ III}]\lambda 5007$ flux. This indicates that regions within J0919 that have the highest Mg II relative to $[O\text{ III}]$ emission are also the most ionized. We find similar trends with the $[\text{Ne III}]\lambda 3869/[O\text{ II}]\lambda 3728$ flux ratios (see Ta-

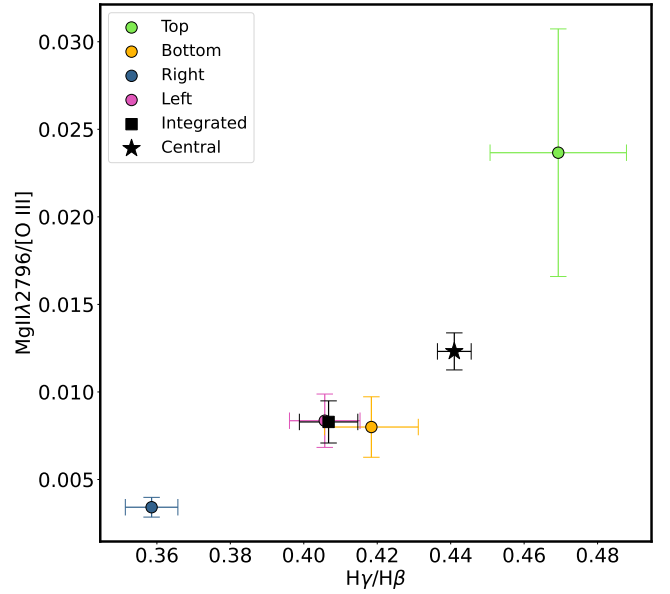


Figure 5. The $H\gamma/H\beta$ flux ratio of the different apertures versus the Mg II λ 2796 flux, normalized by the $[O\text{ III}]\lambda 5007$ flux. The $H\gamma/H\beta$ flux ratio traces dust attenuation and has an intrinsic value of 0.47 in the absence of dust. Regions within J0919 with the highest observed Mg II/ $[O\text{ III}]\lambda 5007$ ratios also have the lowest dust attenuation. The legend caption refers to the aperture location within J0919.

ble 2) but use the $[O\text{ III}]\lambda 5007/[O\text{ II}]\lambda 3728$ ratio because $[O\text{ III}]\lambda 5007$ has significantly higher SNR than $[\text{Ne III}]\lambda 3869$.

The central and integrated apertures are included in our measurements because of the extra information they provide. The central aperture is where the HST/COS observations of the LyC are for J0919. It also represents the Mg II λ 2796 escape fraction of the region where the most ionizing photons are produced. From Figure 6, we see that the central aperture is more transparent in its emission of Mg II λ 2796 flux than the average for J0919, but it is not as transparent as the top aperture. The integrated aperture represents the "total" Mg II escape of J0919. The Mg II λ 2796 escape fraction of the integrated aperture is nearly the average of all the other apertures.

5 DISCUSSION

In this section we explore the differences in our different apertures using the quantities in Tables 1 and 2. We also discuss the implications of the trends between dust, ionization, and Mg II from section 4 on the escape of Mg II and LyC photons.

5.1 Ionization, dust, and escape fractions

To better understand how Mg II serves as a means to trace neutral H and the escape of ionizing photons, we study the spatial variation of Mg II. Confirming methods to infer the LyC escape fraction locally, would allow us to determine how the distant universe was reionized. In Section 4, we show that there are significant relations between the Mg II emission and both the nebular ionization and the dust attenuation. These correlations suggest that a larger fraction of Mg II escapes regions of higher ionization and lower dust attenuation (Figure 5, Figure 6). Both of these conditions are consistent with Mg II being a strong tracer of LyC escape because both dust

Table 1. E(B-V) values, attenuation corrected integrated fluxes, and observed integrated fluxes for 6 different apertures and 9 different emission lines. The fluxes are in units of (10^{-16} erg s $^{-1}$ cm $^{-2}$). E(B-V) is in units of magnitudes. Cor indicates that the values have been attenuation corrected. The aperture naming convention refers to the aperture's position relative to the galaxy's center (see legend of Figure 2) where the integrated aperture is the largest aperture in Figure 1.

Region	E(B-V)	Mg II λ 2796	Mg II λ 2803	[O II] λ 3728	[Ne III] λ 3869	H γ	[O III] λ 4363	H β	[O III] λ 5007
Integrated	-	1.2 \pm 0.1	0.48 \pm 0.01	3.23 \pm 0.05	3.35 \pm 0.04	2.95 \pm 0.05	9.0 \pm 0.5	7.26 \pm 0.08	61.40 \pm 0.09
Integrated ^{Cor}	0.26 \pm 0.04	6 \pm 1	2.3 \pm 0.7	11 \pm 2	11 \pm 2	8.6 \pm 1.3	2.6 \pm 0.4	18 \pm 2	150 \pm 18
Top	-	0.19 \pm 0.03	0.14 \pm 0.04	0.34 \pm 0.02	0.43 \pm 0.01	0.38 \pm 0.01	0.12 \pm 0.01	0.81 \pm 0.02	7.38 \pm 0.04
Top ^{Cor}	0.00 \pm 0.07	0.2 \pm 0.1	0.16 \pm 0.08	0.4 \pm 0.1	0.5 \pm 0.2	0.4 \pm 0.1	0.13 \pm 0.04	0.9 \pm 0.2	7.8 \pm 1.9
Bottom	-	0.21 \pm 0.02	0.10 \pm 0.07	0.70 \pm 0.02	0.73 \pm 0.02	0.62 \pm 0.02	0.24 \pm 0.02	1.48 \pm 0.03	12.91 \pm 0.03
Bottom ^{Cor}	0.21 \pm 0.06	0.8 \pm 0.3	0.4 \pm 0.3	1.9 \pm 0.5	1.9 \pm 0.5	1.5 \pm 0.3	0.6 \pm 0.1	3.1 \pm 0.6	26 \pm 5
Right	-	0.29 \pm 0.03	0.11 \pm 0.05	0.81 \pm 0.02	0.82 \pm 0.01	0.74 \pm 0.01	0.23 \pm 0.01	2.06 \pm 0.03	15.95 \pm 0.03
Right ^{Cor}	0.50 \pm 0.04	5 \pm 1	2 \pm 1	8 \pm 1	8 \pm 1	5.5 \pm 0.8	1.7 \pm 0.3	12 \pm 2	85 \pm 10
Left	-	0.24 \pm 0.03	0.11 \pm 0.06	0.70 \pm 0.02	0.72 \pm 0.01	0.61 \pm 0.01	0.17 \pm 0.01	1.51 \pm 0.01	11.96 \pm 0.03
Left ^{Cor}	0.26 \pm 0.05	1.2 \pm 0.3	0.5 \pm 0.3	2.4 \pm 0.5	2.5 \pm 0.5	1.8 \pm 0.3	0.5 \pm 0.1	3.9 \pm 0.6	30 \pm 4
Central	-	0.40 \pm 0.02	0.14 \pm 0.02	1.25 \pm 0.02	1.29 \pm 0.01	1.22 \pm 0.01	0.41 \pm 0.01	2.76 \pm 0.01	21.87 \pm 0.03
Central ^{Cor}	0.10 \pm 0.02	0.8 \pm 0.1	0.27 \pm 0.05	2.2 \pm 0.2	2.2 \pm 0.2	2.0 \pm 0.2	0.66 \pm 0.05	4.2 \pm 0.3	33 \pm 2

Table 2. Emission line flux ratios for the 6 different apertures. All fluxes are dust extinction corrected except for the Mg II, H α /H β , and H γ /H β ratios.

Region	Mg II λ 2796/Mg II λ 2803	[O III] λ 5007/[O II] λ 3728	Mg II λ 2796/[O III] λ 5007	[Ne III] λ 3869/[O II] λ 3728	H γ /H β	12+log(O/H)
Integrated	2.6 \pm 0.6	13.6 \pm 0.4	0.008 \pm 0.001	1.006 \pm 0.03	0.407 \pm 0.008	8.02 \pm 0.07
Top	1.3 \pm 0.4	21.3 $^{+0.6}_{-0.7}$	0.024 \pm 0.007	1.3 $^{+0.1}_{-0.09}$	0.47 \pm 0.02	8.1 \pm 0.1
Bottom	2 \pm 1	14.0 $^{+0.6}_{-0.7}$	0.008 \pm 0.002	1.01 \pm 0.04	0.42 \pm 0.01	7.9 \pm 0.1
Right	2.7 \pm 1.4	10.6 \pm 0.3	0.0034 \pm 0.0006	0.97 \pm 0.03	0.359 \pm 0.007	7.90 \pm 0.07
Left	2.3 \pm 1.4	12.1 $^{+0.3}_{-0.4}$	0.008 \pm 0.002	1.002 $^{+0.04}_{-0.03}$	0.41 \pm 0.01	8.0 \pm 0.1
Central	3.0 \pm 0.5	15.0 \pm 0.1	0.012 \pm 0.001	1.01 \pm 0.02	0.441 \pm 0.005	7.92 \pm 0.04

Table 3. Values from our measurements in the LRS2 2'' aperture and the SDSS spectra. The 2'' aperture is the central aperture in Figure 1. No fluxes have been dust corrected and the E(B-V) values were calculated using Equation 3.

Instrument	H γ /H β	H γ /H β E(B-V)	Mg II λ 2796/Mg II λ 2803	H α /H β	[O III] λ 5007/[O II] λ 3728	[O III] λ 5007/[O III] λ 4959
LRS2 2''	0.441 \pm 0.005	0.11 \pm 0.02	3.0 \pm 0.5	3.95 \pm 0.02	17.4 \pm 0.2	3.11 \pm 0.01
SDSS	0.44 \pm 0.01	0.10 \pm 0.06	1.9 \pm 0.5	2.97 \pm 0.03	12.3 \pm 0.3	3.05 \pm 0.02

Table 4. Values from our measurements of the Mg II and LyC escape fractions along with the ionizing photon escape estimate, $F_{\text{escLyC}} * F(\text{H}\beta)$, for the 6 individual apertures and the average of the spatially distinct regions. All the escape fractions are percentages. $F(\text{H}\beta)$ is the extinction corrected H β flux. $F_{\text{escLyC}} * F(\text{H}\beta)$ has units of (10^{-18} erg s $^{-1}$ cm $^{-2}$), except for the Average value. The average is weighted by $F(\text{H}\beta)$, making it unitless.

Region	Mg II Escape	LyC Escape	$F_{\text{escLyC}} * F(\text{H}\beta)$
Integrated	34 \pm 6	0.2 \pm 0.2	4 \pm 3
Top	100 \pm 50	100 \pm 210	90 \pm 180
Bottom	34 \pm 8	0.6 \pm 0.7	2 \pm 2
Right	11 \pm 2	0.0008 \pm 0.0006	0.009 \pm 0.007
Left	32 \pm 7	0.2 \pm 0.2	0.8 \pm 0.8
Central	56 \pm 5	8 \pm 3	32 \pm 13
Average	44 \pm 3	0.3 \pm 0.5	0.05 \pm 0.09

and low-ionization (neutral) gas absorbs ionizing photons (Chisholm et al. 2020). These empirical trends suggest that more Mg II photons, and by extension LyC photons, will escape highly ionized and dust free regions. This would be expected if Mg II emission arises in regions that are transparent to LyC photons. We can extend this analysis further by calculating the Mg II escape fractions from the Mg II/[O III] λ 5007 ratio and the photoionization models from Henry et al. (2018).

To calculate the Mg II escape fractions, we used equa-

tion 1 from Henry et al. (2018) and our dust attenuation corrected [O III] λ 5007/[O II] λ 3728 ratio to calculate the intrinsic Mg II λ 2796/[O III] λ 5007 ratio. We calculated our observed Mg II λ 2796/[O III] λ 5007 ratio with the observed Mg II λ 2796 flux and the dust attenuation corrected [O III] λ 5007 flux. The ratio of our observed value to the intrinsic value is our reported Mg II escape fraction. Combining Figure 5 and Figure 6, we find that regions of low dust attenuation that are highly ionized emit roughly 100% of their intrinsic Mg II emission, while regions that are lower ionization and higher dust attenuation emit \sim 10% of their intrinsic Mg II emission. This factor of \sim 10 difference in Mg II escape fraction illustrates that there are strong spatial variations in the Mg II escape (we discuss this more in the next section).

Finally, we follow Chisholm et al. 2020 to extend the Mg II escape fraction to the LyC escape fraction by dust correcting the Mg II escape fraction (Table 4). To do this, we convert the E(B-V) that was inferred using the Cardelli attenuation curve to one using the Reddy et al. 2016 reddening curve and then use the value of the Reddy et al. 2016 attenuation law at 912 ($k(912) = 12.87$). Since regions with high dust attenuation already have lower Mg II escape fractions, these regions can have five orders of magnitude lower LyC escape fractions. The high dust attenuation and low ionization (more neutral gas) of these regions compound to reduce the LyC escape fractions.

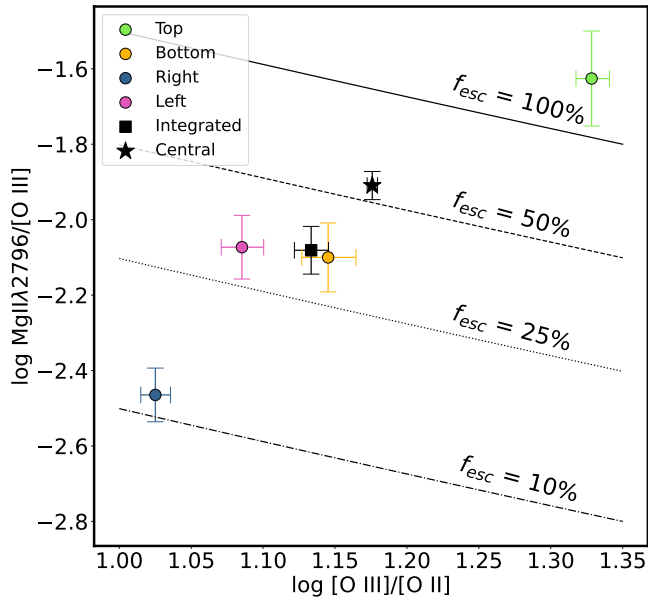


Figure 6. The ionization of the galaxy measured with the $[\text{O III}]\lambda 5007/[\text{O II}]\lambda 3728$ ratio versus the $\text{Mg II}\lambda 2796$ flux, normalized by the $[\text{O III}]\lambda 5007$ flux. The lines represent different $\text{Mg II}\lambda 2796$ escape fractions (Henry et al. 2018). Regions within J0919 with the highest ionization have the largest Mg II escape fractions. The legend caption refers to the aperture location.

Some sightlines through the same galaxy are either transparent or opaque to ionizing photons.

In summary, we find that regions within J0919 that are highly ionized and have low dust attenuation emit a larger fraction of their intrinsic Mg II , and by extension LyC, photons. The strong correlations found in Figures 4, 5, and 6 illustrate the conditions that are likely to lead to LyC escape are intimately intertwined: low-dust and highly ionized regions within galaxies will have the greatest amounts of Mg II emission.

5.2 Variations between apertures

Recent observations have successfully found local galaxies that emit ionizing photons. These observations have found escape fractions between 0-73%, with a large scatter in many of the classically expected diagnostics – like $[\text{O III}]\lambda 5007/[\text{O II}]\lambda 3728$ and $\text{H}\beta$ equivalent widths (Naidu et al. 2018; Fletcher et al. 2019; Izotov et al. 2021). To reconcile these observations with a complete understanding of Reionization would require a measurement of the volume-averaged escape fraction from LyC leakers. However, all of the direct LyC detections are along a single sight-line and do not represent a volume-averaged LyC escape fraction. Three important questions arise from this fact: (a) How can we interpret single sight-line LyC escape observations? (b) How representative of a volume-averaged escape fraction is a single LyC detection? (c) Can spatial variations in the LyC escape lead to the scatter observed in the indirect estimators of LyC escape?

In Figure 6, we observe significant spatial variations in the Mg II escape fractions in J0919. Previous work suggests that if we dust correct the Mg II escape fraction it can predict the LyC escape fractions (see subsection 5.1; Henry et al. 2018; Chisholm et al. 2020). Since the dust attenuates LyC photons more than Mg II photons and is also correlated with the $\text{Mg II}/[\text{O III}]$ ratio (Figure 5), this means that the

LyC escape fraction varies spatially even more dramatically than the Mg II escape fraction. Izotov et al. 2021 measured a LyC escape fraction of 16% along a single line of sight through the central portion of J0919. This value is consistent with the LyC escape fraction we infer from the central region of J0919. Intriguingly, our Mg II and dust observations imply that if we could measure the LyC escape fraction from a different line of sight within J0919, we would likely infer significantly different LyC escape values. For example, from the values in Table 4, the top and left apertures differ by a factor of 10 in their Mg II escape fraction. Given that dust preferentially absorbs shorter wavelengths, dust correcting the Mg II escape fractions implies that the LyC escape fractions differ by six orders of magnitude. More concretely, the LyC escape fraction in the right aperture is 0.0008%, while it is approximately 100% in the upper aperture. It appears that some sight-lines out of J0919 are both optically thin and optically thick to ionizing photons. This suggests that LyC escape fractions are highly sight-line dependent. Sight-line to sight-line variations could introduce significant scatter to both indirect and direct estimates of LyC escape.

Indirect measurements of LyC escape fractions, such as $[\text{O III}]/[\text{O II}]$, may have their abilities to predict LyC escape fractions greatly weakened by the scatter introduced by single sight-line observations. To quantify this scatter we take the average of the Mg II and LyC escape fractions from all the spatially distinct regions (Top, Bottom, Right, and Left; see Table 4). From the averages, we estimate that single sight-line observations of LyC escape can vary from three to six orders of magnitude around the average value. In stark contrast to this, there is only a factor of 2 difference in the $[\text{O III}]/[\text{O II}]$ values. This fact implies that at fairly constant $[\text{O III}]/[\text{O II}]$ values, the line of sight LyC escape fractions can take on huge differences in value. Recovering any trends from this amount of scatter would require very large samples.

The Integrated aperture can alleviate the scatter because it does agree with the average within 1σ and can thus provide an estimate of the galaxy as a whole. With the Integrated aperture and the midpoint of the scatter being very similar, one can possibly estimate the integrated escape fraction from the scatter in observations. While the Integrated aperture does not represent the "volume-averaged" escape fraction because we do not see the backside of the galaxy, it does approximate the average escape fraction of the side of the galaxy we see.

The central aperture, the brightest and one of the most transparent regions, represents the type of region that is most likely to be probed with single sight-line observations. This region is where the LyC measurement from Izotov et al. 2021 was made. The question is then, how well does our brightest region represent the total escape fraction of the galaxy? The central aperture has ~ 1.5 times higher Mg II escape fraction and ~ 40 times higher LyC escape fraction when compared to both the integrated aperture and the average escape fraction of all the regions. A single sight-line observation, especially one of a bright commonly probed region, can result in over, or under, predictions of the average escape fraction of a galaxy (e.g. the Central region and the Right region, respectively). Single sight-line observations on scales smaller than the total galaxy could introduce the significant LyC escape fraction variations that we estimate in J0919. Observing different sight-lines reduces the relatively large, and cosmically-relevant, escape fraction of $\sim 10\%$ in the center to be less than 1% over the whole galaxy. Thus, even if a single sight-lines implies large LyC escape fractions, the entire galaxy may not be emitting sufficient ionizing photons to reionize the Universe.

While a single sight-line observation may not produce escape fractions that are representative of the entire galaxy, we can produce

estimates of the total amount of reionization-powering photons that escape J0919 to test the single sight-line observation. To produce this estimate, we multiply the extinction-corrected $H\beta$ flux ($F(H\beta)$) by the LyC escape fraction for each of the individual regions. This technique can trace reionization because in regions where an electron is ionized off its proton there will be another free proton for the electron to recombine with and emit a recombination line such as $H\beta$. From only the flux values in Table 1, one might expect that the Central region would dominate in total ionizing photons given that it has four times more $F(H\beta)$ than the Top region. However, the Top region emits seven times more of its ionizing photons than the Central region. This transparency makes the Top region the largest total emitter of ionizing photons. A caveat to this technique is that in regions that are very optically thin, like the Top region, the ionizing photons will escape and not ionize the hydrogen, thus reducing the amount of $F(H\beta)$. Our estimate of the total ionizing photons from the Top region may be lower than the actual value because of this. Unlike with the escape fractions, our average for this parameter is weighted by the $H\beta$ flux. Weighting by this value ensures that the average is pulled towards regions with larger production of ionizing photons. There is a scatter of five orders of magnitude around the average value and no single sight-line observation predicts the average.

As was the case with the escape fractions, this photon count varies strongly spatially (five orders of magnitude). From our estimates of the escape fractions and the photon counts, we can return to the three questions posed above: (a) Single sight-line observations do not necessarily provide the escape fraction of an entire galaxy. (b) A single LyC detection does not represent a "volume-averaged" escape fraction and a single sight-line can produce dramatically different escape fractions from a "volume-average". (c) Spatial variation in LyC escape leads to scatter in indirect estimators of LyC escape.

6 SUMMARY AND CONCLUSIONS

In this paper we presented LRS2 spatially resolved spectroscopic observations of $Mg\ II\lambda 2796$, $Mg\ II\lambda 2803$, $[O\ II]\lambda 3728$, $[Ne\ III]\lambda 3869$, $H\gamma$, $[O\ III]\lambda 4363$, $H\beta$, $[O\ III]\lambda 4959$, $[O\ III]\lambda 5007$, and $H\alpha$ from the previously confirmed LyC emitting galaxy, J0919+4906. J0919+4906 has an ionizing photon escape fraction of 16%.

In order to test the spatial variation of $Mg\ II$ emission, dust attenuation, and nebular ionization, we separated our data into four spatially distinct apertures and one large aperture to contain all of the signal from our galaxy. We include a central aperture to capture the brightest region of the galaxy and to compare our methods to the literature. This central region is where the LyC detection was made in Izotov et al. 2021. The spatially distinct apertures were separated by more than the convolved seeing of the observations (1.25 arcsec; Figure 1). To calculate the emission line properties, we fit a single Gaussian to all the line profiles from the aperture-extracted spectra (Figure 3). We use the observed Balmer ratios in order to dust attenuation correct our fluxes to have intrinsic values with which to calculate metallicities and escape fractions (Table 2; Table 1).

We observe spatial variations in $Mg\ II$ emission taken relative to $[O\ III]\lambda 5007$, dust attenuation, and nebular ionization (Figures 4, 5, and 6). More specifically we find: regions with less dust attenuation are more ionized; regions with more $Mg\ II$ flux relative to $[O\ III]\lambda 5007$ are more highly ionized and have less dust attenuation.

From our values for ionization and $Mg\ II$ emission taken relative to $[O\ III]\lambda 5007$, we use photoionization models to calculate the escape fraction of $Mg\ II$. We find that there is large spatial variation in the $Mg\ II$ escape fraction (Table 4). From these variations we find that

regions with low dust attenuation and high ionization will have more $Mg\ II$ emission escape. In subsection 5.2 we dust correct the $Mg\ II$ escape fractions to estimate the LyC escape fractions. The regions with low $Mg\ II$ escape, due to the strong correlation between $Mg\ II$ and dust, have even lower LyC escape fractions. Single-sightline observations may not accurately reflect the volume averaged LyC escape fraction.

We find that the Integrated aperture, which contains all of the signal from the galaxy, represents the average $Mg\ II$ and LyC escape fractions of the spatially distinct apertures. The central aperture is the brightest region and thus the region that is most often probed in observations. For example, the direct LyC observation from Izotov et al. 2021 was done on this region of the galaxy. The LyC escape fraction from this region is an order of magnitude higher than the average for this galaxy. This places the average of the galaxy below the typically-quoted value needed to reionize the universe and the central value above this limit. The variability in the values of each sight-line also introduces scatter in the indirect estimators of LyC escape. With this information, we determine that a single sight-line on scales smaller than the entire galaxy is not enough to infer the escape fraction of a galaxy.

ACKNOWLEDGEMENTS

We would like to acknowledge that the HET is built on Indigenous land. Moreover, we would like to acknowledge and pay our respects to the Carrizo & Comecrudo, Coahuiltecan, Caddo, Tonkawa, Comanche, Lipan Apache, Alabama-Coushatta, Kickapoo, Tigua Pueblo, and all the American Indian and Indigenous Peoples and communities who have been or have become a part of these lands and territories in Texas, here on Turtle Island.

The Hobby-Eberly Telescope (HET) is a joint project of the University of Texas at Austin, the Pennsylvania State University, Ludwig-Maximilians-Universität München, and Georg-August-Universität Göttingen. The HET is named in honor of its principal benefactors, William P. Hobby and Robert E. Eberly.

The Low Resolution Spectrograph 2 (LRS2) was developed and funded by the University of Texas at Austin McDonald Observatory and Department of Astronomy and by Pennsylvania State University. We thank the Leibniz-Institut für Astrophysik Potsdam (AIP) and the Institut für Astrophysik Göttingen (IAG) for their contributions to the construction of the integral field units.

DATA AVAILABILITY

The data underlying this article will be shared on request to the corresponding author.

REFERENCES

- Aguado D. S., et al., 2019, *ApJS*, **240**, 23
- Astropy Collaboration et al., 2018, *AJ*, **156**, 123
- Bañados E., et al., 2017, *Nature*, **553**, 473–476
- Becker R. H., et al., 2001, *The Astronomical Journal*, **122**, 2850
- Berg D. A., 2013, PhD thesis, University of Minnesota, United States
- Cardelli J. A., Clayton G. C., Mathis J. S., 1989, *ApJ*, **345**, 245
- Chisholm J., et al., 2018, *Astronomy & Astrophysics*, **616**, A30
- Chisholm J., Prochaska J. X., Schaerer D., Gazagnes S., Henry A., 2020, *MNRAS*, **498**, 2554
- Chonis T. S., Hill G. J., Lee H., Tuttle S. E., Vattiat B. L., 2014, *Ground-based and Airborne Instrumentation for Astronomy V*

- Fan X., et al., 2006, *The Astronomical Journal*, 132, 117
- Faucher-Giguère C.-A., Lidz A., Zaldarriaga M., Hernquist L., 2009, *The Astrophysical Journal*, 703, 1416–1443
- Finkelstein S. L., et al., 2019, *The Astrophysical Journal*, 879, 36
- Fletcher T. J., Tang M., Robertson B. E., Nakajima K., Ellis R. S., Stark D. P., Inoue A., 2019, *The Astrophysical Journal*, 878, 87
- Garnett D. R., 1992, *AJ*, 103, 1330
- Gazagnes S., Chisholm J., Schaerer D., Verhamme A., Rigby J. R., Bayliss M., 2018, *Astronomy & Astrophysics*, 616, A29
- Gazagnes S., Koopmans L. V. E., Wilkinson M. H. F., 2021, *Monthly Notices of the Royal Astronomical Society*, 502, 1816–1842
- González Delgado R. M., Leitherer C., Heckman T. M., 1999, *ApJS*, 125, 489
- Green G. M., Schlafly E., Zucker C., Speagle J. S., Finkbeiner D., 2019, *The Astrophysical Journal*, 887, 93
- Grimes J. P., et al., 2009, *The Astrophysical Journal Supplement Series*, 181, 272
- Harris C. R., et al., 2020, *Nature*, 585, 357
- Henry A., Berg D. A., Scarlata C., Verhamme A., Erb D., 2018, *The Astrophysical Journal*, 855, 96
- Hopkins P. F., Hernquist L., Cox T. J., Kereš D., 2008, *The Astrophysical Journal Supplement Series*, 175, 356–389
- Izotov Y. I., Worseck G., Schaerer D., Guseva N. G., Thuan T. X., Fricke Verhamme A., Orlitová I., 2018, *Monthly Notices of the Royal Astronomical Society*, 478, 4851
- Izotov Y. I., Worseck G., Schaerer D., Guseva N. G., Chisholm J., Thuan T. X., Fricke K. J., Verhamme A., 2021, *Monthly Notices of the Royal Astronomical Society*, 503, 1734–1752
- Jaskot A. E., Dowd T., Oey M. S., Scarlata C., McKinney J., 2019, *The Astrophysical Journal*, 885, 96
- Kramida A., Yu. Ralchenko Reader J., and NIST ASD Team 2021, NIST Atomic Spectra Database (ver. 5.9), [Online]. Available: <https://physics.nist.gov/asd> [2017, April 9]. National Institute of Standards and Technology, Gaithersburg, MD.
- Leitherer C., Hernandez S., Lee J. C., Oey M. S., 2016, *The Astrophysical Journal*, 823, 64
- Luridiana V., Morisset C., Shaw R. A., 2014, *Astronomy & Astrophysics*, 573, A42
- Madau P., Dickinson M., 2014, *Annual Review of Astronomy and Astrophysics*, 52, 415–486
- Madau P., Haardt F., 2015, *The Astrophysical Journal*, 813, L8
- Matsuoka Y., et al., 2018, *The Astrophysical Journal*, 869, 150
- Matthee J., et al., 2021, (Re)Solving Reionization with $\text{Ly}\alpha$: *How Bright $\text{Ly}\alpha$ Emitters account for the $z \approx 2 - 8$ Cosmic Ionizing Background* ([arXiv:2110.11967](https://arxiv.org/abs/2110.11967))
- Naidu R. P., Forrest B., Oesch P. A., Tran K.-V. H., Holden B. P., 2018, *MNRAS*, 478, 791
- Naidu R. P., Tacchella S., Mason C. A., Bose S., Oesch P. A., Conroy C., 2020, *The Astrophysical Journal*, 892, 109
- Nakajima K., Ouchi M., 2014, *Monthly Notices of the Royal Astronomical Society*, 442, 900–916
- Newville M., Stensitzki T., Allen D. B., Ingargiola A., 2014, LMFIT: Non-Linear Least-Square Minimization and Curve-Fitting for Python, [doi:10.5281/zenodo.11813](https://doi.org/10.5281/zenodo.11813), <https://doi.org/10.5281/zenodo.11813>
- Oesch P. A., et al., 2009, *The Astrophysical Journal*, 709, L16–L20
- Oey M. S., Pellegrini E. W., Zastrow J., Jaskot A. E., 2014, Ionization by Massive Young Clusters as Revealed by Ionization-Parameter Mapping ([arXiv:1401.5779](https://arxiv.org/abs/1401.5779))
- Onoue M., et al., 2017, *The Astrophysical Journal*, 847, L15
- Osterbrock D. E., 1989, Astrophysics of gaseous nebulae and active galactic nuclei
- Ouchi M., et al., 2009, *The Astrophysical Journal*, 706, 1136–1151
- Reddy N. A., Steidel C. C., Pettini M., Bogosavljević M., 2016, *ApJ*, 828, 107
- Ricci F., Marchesi S., Shankar F., La Franca F., Civano F., 2016, *Monthly Notices of the Royal Astronomical Society*, 465, 1915
- Rivera-Thorsen T. E., et al., 2017, *Astronomy & Astrophysics*, 608, L4
- Robertson B. E., et al., 2013, *The Astrophysical Journal*, 768, 71
- Robertson B. E., Ellis R. S., Furlanetto S. R., Dunlop J. S., 2015, *The Astrophysical Journal*, 802, L19
- Rosa-González D., Terlevich E., Terlevich R., 2002, *Monthly Notices of the Royal Astronomical Society*, 332, 283–295
- Shen X., Hopkins P. F., Faucher-Giguère C.-A., Alexander D. M., Richards G. T., Ross N. P., Hickox R. C., 2020, *Monthly Notices of the Royal Astronomical Society*, 495, 3252
- Smee S. A., et al., 2013, *The Astronomical Journal*, 146, 32
- Steidel C. C., Bogosavljević M., Shapley A. E., Reddy N. A., Rudie G. C., Pettini M., Trainor R. F., Strom A. L., 2018, *The Astrophysical Journal*, 869, 123
- Vanzella E., et al., 2010, *The Astrophysical Journal*, 725, 1011
- Verhamme A., Orlitová I., Schaerer D., Hayes M., 2015, *Astronomy & Astrophysics*, 578, A7
- Wang T., et al., 2019, *Nature*, 572, 211–214
- Witstok J., Smit R., Maiolino R., Curti M., Laporte N., Massey R., Richard J., Swinbank M., 2021, *Monthly Notices of the Royal Astronomical Society*, 508, 1686–1700

This paper has been typeset from a \LaTeX file prepared by the author.